

Article

Gold and Ceria Modified NiAl Hydrotalcite Materials as Catalyst Precursors for Dry Reforming of Methane

Valeria La Parola ¹, Giuseppe Pantaleo ^{1,*}, Leonarda Francesca Liotta ¹, Anna Maria Venezia ^{1,*}, Margarita Gabrovska ², Dimitrinka Nikolova ² and Tatyana Tabakova ^{2,*}¹ Istituto per lo Studio dei Materiali Nanostrutturati, CNR, 90146 Palermo, Italy² Institute of Catalysis, Bulgarian Academy of Sciences, 1113 Sofia, Bulgaria

* Correspondence: giuseppe-pantaleo@cnr.it (G.P.); annamaria.venezia@cnr.it (A.M.V.); tabakova@ic.bas.bg (T.T.)

Abstract: Structured hydrotalcite NiAl-HT material with Ni/Al atomic ratio of 2.5 was prepared by co-precipitation of Ni and Al nitrate precursors and then modified by the addition of 1 wt% Ce and/or 3 wt% Au species. The obtained materials, after calcination at 600 °C, were characterized by XRD, XPS and TPR. Their catalytic performance was tested through dry reforming of methane (DRM) and by the temperature-programmed surface reaction of methane (TPSR-CH₄). Thermal gravimetry analysis (TGA) of the spent catalysts was performed to determine the amount of carbon accumulated during the reaction. The effects of the addition of cerium as a support promoter and gold as nickel promoter and the sequential addition of cerium and gold on the structural properties and on the catalytic efficiency were investigated. Under the severe condition of high space velocity (600,000 mL g⁻¹ h⁻¹), all the catalysts were quite active, with values of CH₄ conversion between 67% and 74% at 700 °C. In particular, the combination of cerium and gold enhanced the CH₄ conversion up to 74%. Both additives, individually and simultaneously, enhanced the nickel dispersion with respect to the unpromoted NiAl and favored the reducibility of the nickel. During DRM all the catalysts formed graphitic carbon, contributing to their deactivation. The lower carbon gasification temperature of the promoted catalysts confirmed a positive effect played by Ce and Au in assisting the formation of an easier-to-remove carbon. The positive effect was testified by the better stability of the Ce/NiAl with respect to the other catalysts. In the gold-containing samples, this effect was neutralized by Au diffusing towards the catalyst surface during DRM, masking the nickel active sites. TPSR-CH₄ test highlighted different CH₄ activation capability of the catalysts. Furthermore, the comparison of the deposited carbon features (amount and removal temperature) of the DRM and TPSR spent catalysts indicated a superior activation of CO₂ by the Au/Ce/NiAl, to be related to the close interaction of gold and ceria enhancing the oxygen mobility in the catalyst lattice.

Keywords: NiAl hydrotalcite catalysts; Au and Ce promoters; dry reforming of methane (DRM)

Citation: La Parola, V.; Pantaleo, G.; Liotta, L.F.; Venezia, A.M.; Gabrovska, M.; Nikolova, D.; Tabakova, T. Gold and Ceria Modified NiAl Hydrotalcite Materials as Catalyst Precursors for Dry Reforming of Methane. *Catalysts* **2023**, *13*, 606. <https://doi.org/10.3390/catal13030606>

Academic Editor:
Avelina García-García

Received: 17 February 2023

Revised: 10 March 2023

Accepted: 13 March 2023

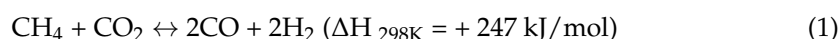
Published: 16 March 2023



Copyright: © 2023 by the authors. Licensee MDPI, Basel, Switzerland. This article is an open access article distributed under the terms and conditions of the Creative Commons Attribution (CC BY) license (<https://creativecommons.org/licenses/by/4.0/>).

1. Introduction

The energetic crisis connected to geopolitical changes and to the continuous depletion of fossil fuels requires the rapid development of efficient renewable energy sources, such as solar, wind and tidal power, green hydrogen and efficient chemical processes, to produce synthetic fuels and chemicals [1]. Among the relevant chemical processes, dry reforming of methane with CO₂ (DRM) is currently the subject of increased attention from the research and industrial community as a prospective method for obtaining fuels and chemicals through the conversion of the syngas produced according to the following equation.



The obtained syngas is a mixture of H₂ and CO in a 1:1 molecular ratio, ideal for the Fischer-Tropsch synthesis of fuels and for the synthesis of oxygenates. Furthermore, the

conversion of CH₄ and CO₂ into a mixture of H₂ and CO, two important chemical precursor molecules, would conceivably contribute to the recycling of the two most green housing effect gases [2–6]. However, the effect of this process in global warming mitigation depends on different factors, such as the source of CO₂, (whether from fossil fuel combustion or from organic waste), or the temperature of the reaction [5,7]. The development of this process at the industrial level is still hampered by the lack of appropriate catalysts with high efficiency and low cost. It is well-recognized that nickel-based catalysts are the most suitable in terms of costs over benefits [6]. Nevertheless, nickel suffers from easy deactivation. The loss of efficiency with time is mainly ascribable to coking and to the sintering of the active nickel sites. Coking is the formation of carbon, which, depending on its morphology and structure, may affect the catalyst activity differently [8]. The formation of carbon graphite, favored by larger nickel particles, is highly detrimental, being rather inert and difficult to gasify, differently from the amorphous carbon, which could be easily removed by subsequent treatment with water (C + H₂O = CO + H₂) or with CO₂ [5,9,10]. Limiting the nickel particle size or using supports with a certain degree of basicity would help to mitigate the coking effects [6]. An inverse relationship between nickel particle sizes and DRM activity was observed with an optimal particle size around 2–3 nm for reaction temperature of 500–600 °C [11,12]. According to literature, the size of the nickel particles plays an important role in the nucleation and growth of carbon filament. Generally, the initiation step for carbon formation is more difficult in small particles, and increasing the size beyond 6 nm generates more carbon [13]. The sintering effect occurring during the pretreatment reduction and during the reaction at high temperature is generally avoided using appropriate support design, suitable catalyst synthesis and the addition of proper promoters. The use of different supports and different synthetic procedures is intended to increase the interaction between the nickel and the carrier to limit the otherwise free particle growth [5]. SiO₂ and Al₂O₃ are the most used supports for this type of catalysts, each having characteristics beneficial to the catalytic activity of the supported nickel [14]. SiO₂, being a non-interacting support, allows an easy reduction of the nickel, but it does not restrain its particle size. On the other hand, Al₂O₃, which is a much more interactive oxide, limits the nickel particle growth but at the same time inhibits the nickel reduction, with a consequent loss of activity. Different types of promoters have been investigated, aiming to favor the reducibility of the catalyst without enhancing metal sintering, or to modify the basicity/acidity property of the carrier to increase the catalytic stability without reducing the activity [15]. The addition of alkali/alkaline metals, increasing the support basicity, would favor the adsorption and activation of the acidic CO₂ molecule, with the consequent gasification of the deposited carbon through the reverse of the Boudouard reaction according to the following equation [6,8].



However, a good compromise between acidity and basicity must be considered, since a certain degree of support acidity is known to favor the CH₄ decomposition and consequently its conversion [6]. The addition of rare earth metals, such as Ce, Zr and La, was demonstrated to improve the catalytic performance by preventing the formation of coke. Ce, with its high oxygen storage capacity (OSC) related to the rapid interchange between the Ce³⁺ and Ce⁴⁺ redox couple, would provide oxygen vacancies promoting CO₂ adsorption and dissociation, increasing the activity of the catalyst and the gasification of the deposited carbon during the DRM reaction [16,17]. La also promoted the formation of small nickel particles and gasification of amorphous carbon deposits [18]. Zr, by a moderate interaction with the support, favored the formation of small nickel particles [19]. Other metal promoters, such as Sn, In and Au, have been investigated. Their role in nickel activity promotion was mostly related to their capability of alloying with nickel and therefore restraining the active crystallite size [20–22]. It is worth noting that discrepancies sometimes observed in literature on the role of each promoter are strictly related to the different experimental procedures used for the catalyst preparation and for the reactivity

tests. Therefore, any general statement must be carefully considered. Besides single oxide carriers, mixed oxides of different structural and morphology properties have also been considered as DRM catalyst supports [15]. Catalysts derived from perovskite precursors and from layered double hydroxides (LDH) have been used in the DRM process [23,24]. These solid structures have been claimed to contribute to the formation of well-dispersed and active metal particles. In particular, the LDH compounds, also known as hydrotalcite-type (HT) compounds, are lamellar metal hydroxides consisting of main layers of divalent and trivalent metal cations and anion interlayers [24]. Recently, a special issue of *Catalysts* was entirely dedicated to the application of these compounds as supports or as catalysts for many different sustainable chemical reactions [25]. The suitability of LDH materials as such and as catalyst precursors lies in the active component dispersion, in their high degree of alkalinity and the possibility of forming oxides with homogeneous mesoporous textures. Moreover, the mixed oxides obtained after calcination are characterized by a large specific surface area due to the removal of anion groups such as CO_3^{2-} and NO_3^{2-} , and better resistance to sintering compared to other supported catalysts [26]. Indeed, the mixed oxides derived from calcined hydrotalcite-like precursors have been shown to stabilize the Ni-active centers [27]. The effect of the Ni/Al atomic ratio, of the calcination temperature and of different promoters on the DRM catalytic performance of HT-derived catalysts was investigated [28–30]. The first pioneer study on the hydrotalcite-derived NiAl oxides confirmed a higher methane-reforming activity of these oxides compared to traditional Ni catalysts [31]. Aiming to enhance the nickel reducibility and the stability of the HT-derived catalysts, the effects of different promoters, such as Ce, La and Rh, were investigated [29,30]. Ceria was investigated because of its peculiar oxygen mobility, favoring gasification of the deposited carbon [29]. Lanthania was found to form oxycarbonate $\text{La}_2\text{O}_2\text{CO}_3$, which, reacting with adsorbed CH_x species, contributed to carbon removal [30]. The same authors demonstrated that rhodium increased the reducibility of the nickel, maintaining the activity for longer time [30]. Based on the above grounds, the present study focused on the combined effect of CeO_2 and Au on the DRM catalytic performance of NiAl HT-derived catalysts. Ceria was selected by virtue of its high oxygen-storage capacity and the related effects described above. On the other hand, gold was chosen because of its high electronegativity and alloying capability, favoring nickel reduction and restraining particle growth [22]. In fact, to the best of our knowledge, the combined effect of these two promoters on a nickel HT-derived catalyst has not yet been reported. Recently, some coauthors of the present study published a study on the catalytic performance of NiAl-HT catalysts modified by CeO_2 and Au in the water–gas shift reaction (WGS) [32]. The innovative approach of the direct deposition of ceria on the NiAl-layered structure was successful for the attainment of well-dispersed CeO_2 particles, which effectively constrained the particle size of the deposited gold. Based on these outcomes, a similar procedure was adopted to prepare NiAl hydrotalcite doped with ceria and gold. To avoid aggregation of ceria and to maintain the HT structure of the precursor, only 1 wt% Ce was considered. The DRM catalytic activity of the obtained samples after high-temperature calcination was evaluated and correlated with structural and electronic properties.

2. Results and Discussions

2.1. Catalytic Results

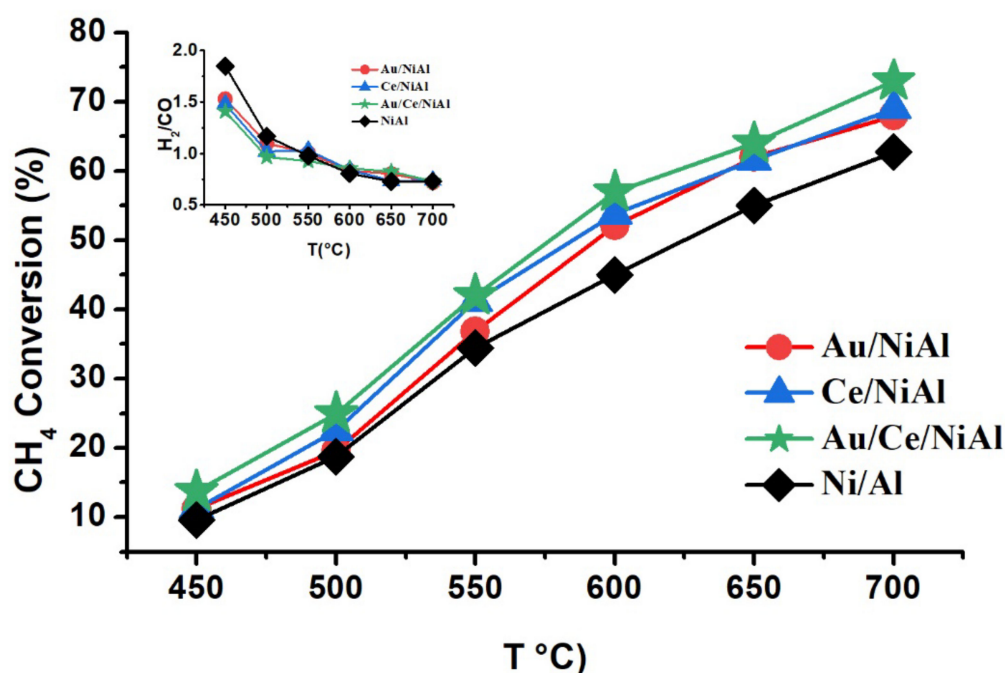
The NiAl-HT-derived catalysts tested in the DRM reaction are listed in Table 1 along with their elemental composition and their textural and structural parameters, which are discussed later.

The CH_4 and CO_2 conversions obtained with the different catalysts, plotted as a function of temperature in the temperature range of 450–700 °C, are shown in Figures 1 and 2, respectively.

Table 1. Elemental composition and textural properties of the HT-derived samples.

Samples	Ni wt%	Al wt%	Ce wt%	Au wt%	S (m ² g ⁻¹)	V _{tot} (cm ³ g ⁻¹)	d _{NiO} * (nm)	d _{Au} (nm)	d _{Ni} ** (nm)
NiAl	61.7	11.3			226	1.00	5(21)		25
Au/NiAl	59.9	11.0		3	215	0.97	4(21)	22	23
CeNiAl	61.1	12.3	0.8		224	0.92	4(12)		16
Au/CeNiAl	59.3	10.9	0.8	3	215	0.97	4(10)	18	20

* The values in parentheses refer to the samples after the DRM catalytic test. ** These values refer to the samples after the DRM catalytic test.

**Figure 1.** CH₄ conversion of NiAl-HT-derived catalysts, with H₂/CO molecular ratio plotted in the inset.

Although a higher reaction temperature favors the DRM reaction and inhibits side reactions, a relatively low temperature range up to 700 °C was selected, being more appealing for economic and technical reasons [4,24]. In the considered temperature range, the values of CH₄ conversion were lower than the thermodynamic equilibrium conversions calculated considering the same conditions of the present study, i.e., at atmospheric pressure and with CH₄/CO₂ ratio of 1, as reported in literature [33]. Conversions of CH₄ between 67% and 74% were obtained at 700 °C under the severe condition of high space velocity (600,000 mL g⁻¹ h⁻¹). These results compared quite positively with those from catalysts of similar composition tested at a much lower-space velocity [24].

A definite improvement in the CH₄ conversion was observed for the Au- and Ce-promoted catalysts, particularly for Au/Ce/NiAl containing both promoter elements as compared to the NiAl. As observed with other nickel-supported catalysts, CO₂ conversions larger than the CH₄ conversions were obtained [34]. The differences, more evident at the lower temperatures, were due to the reverse water-gas shift reaction (RWGS)



competing with the DRM reaction [33,34]. However, the opposite effect of CH₄ conversions larger than the CO₂ conversions was reported with some Ce-promoted hydrotalcite-derived catalysts, attributed to the preferential occurrence of a CH₄ decomposition reaction [24]. Different experimental conditions, such as gas feed dilution or space velocity, might explain

the discrepancy between the results. The H_2/CO molecular ratios, plotted as a function of temperature, are shown in the inset of Figure 1. The ratio decreased with temperature, ranging from values above 1.5 to a stable 0.7 for temperatures above 600 °C, passing through the stoichiometric value of 1 at 550 °C. The changes of the H_2/CO ratio and the discrepancy between CH_4 and CO_2 conversions with temperature were intrinsically related to the side reactions taking place during the DRM test, particularly CH_4 decomposition and RWGS, depending differently on the temperatures [15,33]. Generally, a H_2/CO ratio less than one is due to an excess of CO, which may imply less coke deposition [9,35]. The largest H_2/CO ratio obtained at low temperatures with the unpromoted NiAl catalyst was also in accordance with its superior activity in WGS tested at temperatures up to 300 °C, as reported in the previous study [32].

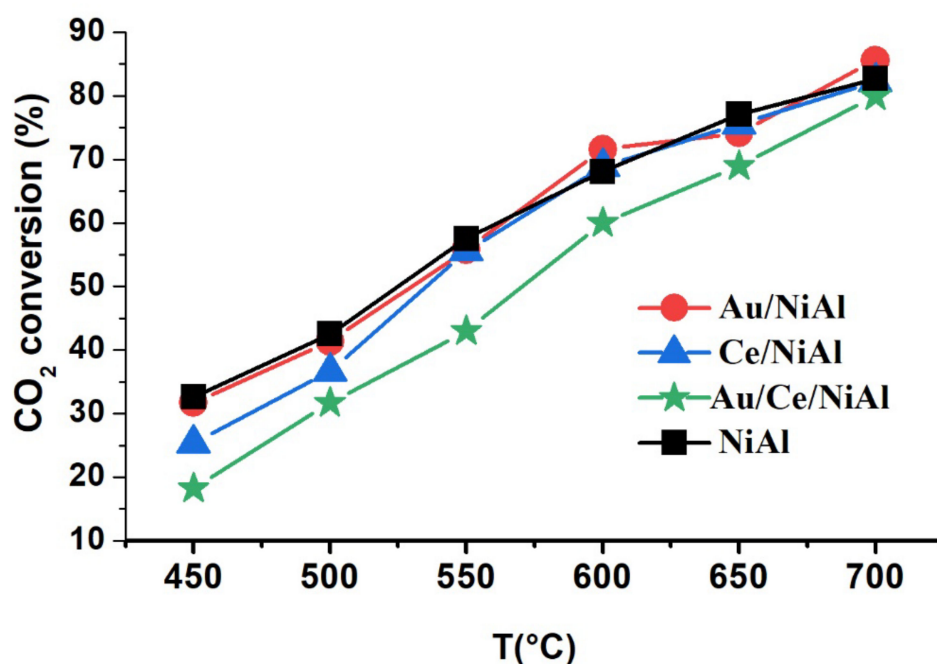


Figure 2. CO_2 Conversion of NiAl-HT-derived catalysts.

At the temperature of 700 °C, the DRM activity of the catalysts was monitored as a function of time on stream (TOS) for 6 h. The obtained conversion plots for CH_4 are displayed in Figure 3.

During the analysis, the H_2/CO atomic ratio maintained a stable value of 0.7. With some differences, all the catalysts deactivated during the 6 h reaction. However, the best stability was exhibited by the Ce/NiAl, and the worst by the two gold-containing catalysts. The deleterious effect of gold relative to the catalyst deactivation was due to the surface migration of gold, covering part of the nickel-active sites. Indeed, the tendency of gold to segregate at the surface of a nickel catalyst upon exposure to the reducing environment at elevated temperature, as in the DRM process, was reported in a previous study on nickel catalysts supported on $MgAl_2O_4$ [22].

For better clarity, the catalytic results at 700 °C in terms of conversion and deactivation percentages, H_2 yield, H_2/CO ratio and percentage of carbon formation discussed below are summarized in Table 2. The hydrogen yield, calculated according to the equation given in the experimental section, ranged from 39% for the unpromoted NiAl to 44% for the gold- and cerium-promoted Au/Ce/NiAl catalyst.

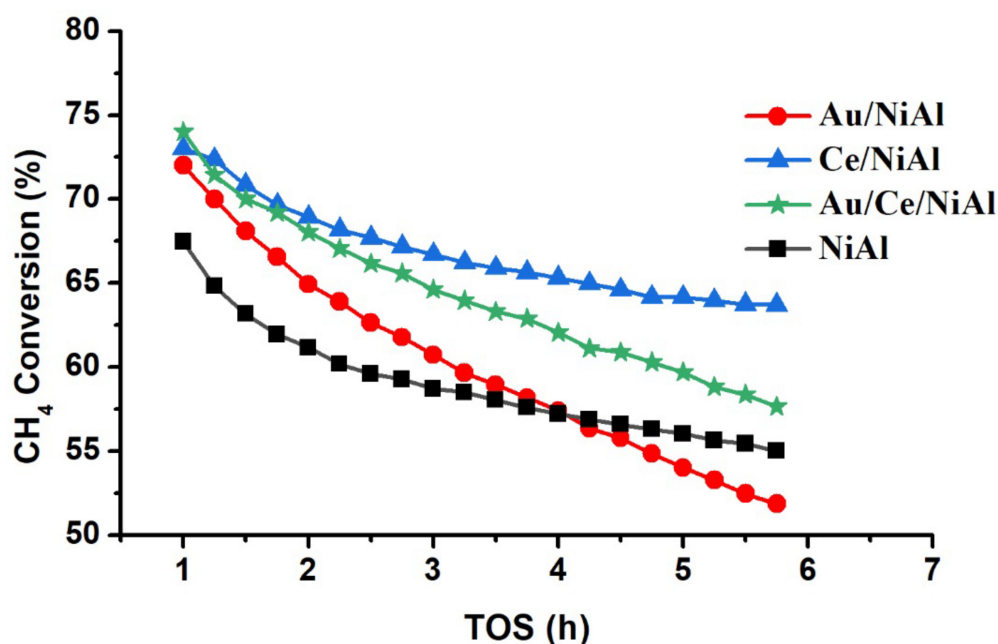


Figure 3. Deactivation test at 700 °C of NiAl-HT-derived catalysts.

Table 2. Catalytic results of DRM at 700 °C for the HT-derived samples, with corresponding TGA-derived carbon information.

Samples	CH ₄ Conversion * (%)	CO ₂ Conversion * (%)	H ₂ Yield * (%)	H ₂ /CO	%C **	T _C *** (°C)
NiAl	67 (19)	83 (07)	39(22)	0.7	244	742
Au/NiAl	72 (28)	86 (08)	43(26)	0.7	244	720
Ce/NiAl	73 (12)	83 (08)	43(10)	0.7	316	704
Au/Ce/NiAl	74 (22)	88 (10)	44(20)	0.7	240	690

* In parentheses, the percentage of decrease after 6 h at 700 °C is given. ** The accumulated carbon during the DRM calculated from TGA weight loss as $(W_i - W_f)/W_f$ (initial weight – final weight)/final weight. *** The DTG temperature peak.

The amount of carbon built up over the samples at the end of the catalytic test was determined by TGA analyses. The profiles are given in Figure 4.

At the beginning of the curves, a slight increase in the weight due to the oxidation of nickel was registered in a temperature range of 200–400 °C. Such an increase, equal for all samples, was hardly detectable, being much smaller compared to the large weight losses due to the carbon combustion. The carbon loss occurred within the wide temperature range of 500–750 °C, which corresponded to the reactivity of different types of carbon [14,27]. According to the profiles of Figure 4 and the calculated percentages of deposited carbon listed in Table 2, a similar amount of carbon formed upon DRM reaction with the unpromoted and promoted samples, except for the Ce-promoted one, which exhibited more carbon formation. Increased carbon deposition for Ce-doped samples was reported on similar types of catalysts and the weight loss observed at temperatures above 600 °C was attributed to graphitic carbon combustion [36]. The first derivative curves (DTG) allowed the pinpointing of the temperatures of the maximum loss, which are also reported in Table 2. Downward temperature shifts of 38 °C for the Ce/NiAl, 22 °C for the Au/NiAl and 52 °C for the Au/Ce/NiAl were observed in comparison to the unpromoted NiAl. The decrease in the temperature confirmed a positive effect exerted by both promoters, favoring the formation of an easier-to-remove carbon [36].

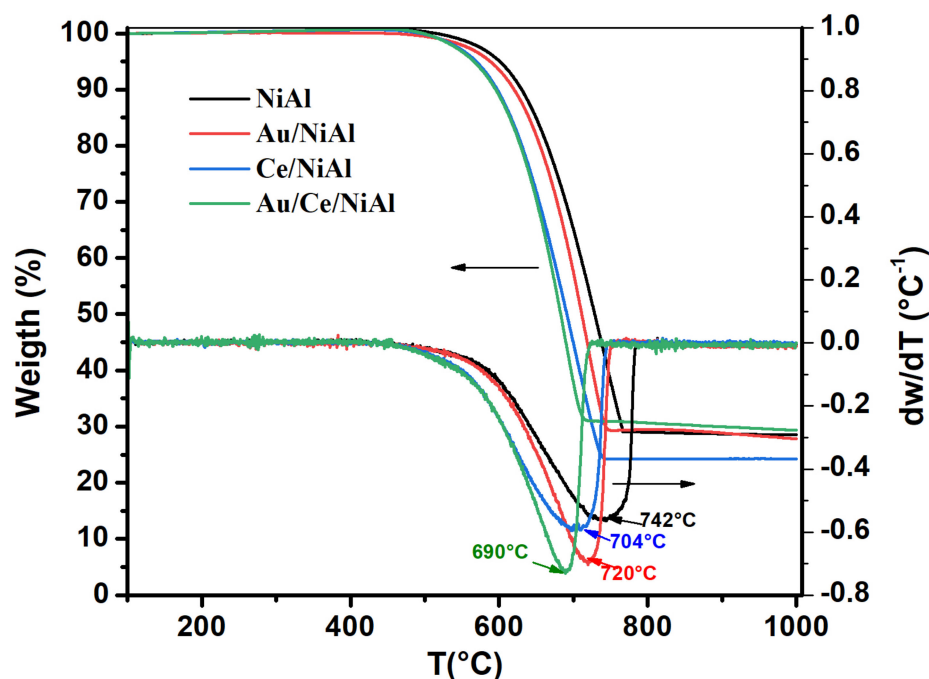


Figure 4. TGA profiles and corresponding DTG profiles of spent NiAl-HT-derived catalysts.

To investigate the activation of methane in the absence of CO_2 by the different samples, the temperature-programmed surface reaction of methane (TPSR- CH_4) method was carried out. The profiles of the gas evolution as a function of temperature are given in Figure 5.

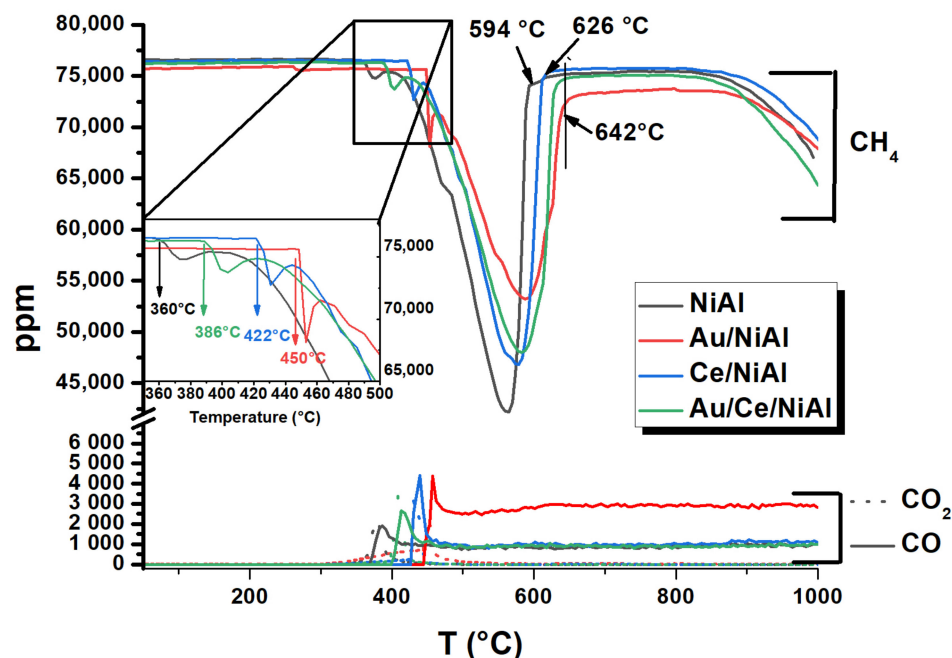


Figure 5. Gas evolution during TPSR- CH_4 over NiAl-HT-derived catalysts.

The start (light off) of the curve with each sample is zoomed in the inset. It is worth noting the presence of small peaks at the beginning of each profile. These peaks corresponded to the conversion of methane reducing the nickel oxide still present on the catalyst surface even after the H_2 pretreatment described in the experimental section. Consequent to this process, CO and CO_2 evolution peaks were registered. The main CH_4 conversion

peaks were due to the decomposition of methane into solid carbon material C(s) and hydrogen gas H₂(g), stoichiometrically evolved with respect to the decomposition reaction of methane [37]. The light-off temperatures, the conversion peak positions, and the decomposition temperature ranges, T_{dec}, summarized in Table 3, reflected the different activation capability of each sample.

Table 3. Catalytic results of CH₄-TPSR test for the HT-derived samples with corresponding TGA-derived carbon information.

Samples	T _{Light-off} (°C)	T _{peak} (°C)	T _{dec range} (°C)	%C *	T _C ** (°C)
NiAl	360	562	234	300	702
Au/NiAl	450	591	194	144	702
Ce/NiAl	422	582	208	426	704
Au/Ce/NiAl	386	584	257	566	732

* The accumulated carbon during TPSR calculated from TGA weight loss as $(W_i - W_f)/W_f$ (initial weight- final weight)/final weight. ** The DTG temperature peak.

As reported in the literature, the temperature window for TPSR-CH₄ activity, corresponding to T_{dec} in Table 3, is indicative of the anti-coking ability in DRM [21,38]. Therefore, according to the T_{dec} values, the Au/Ce/NiAl catalyst should have the best anti-coking aptitude during the dry reforming process in accordance with the TGA results in Table 2 [38]. Simultaneously to the methane decomposition, there is a small but continuous production of CO arising from the reaction of the carbon, stemming from CH₄ dissociation and diffusing through the nickel particles, with the oxygen of the sample lattice [37]. The methane conversion taking place above 800 °C was due to the homogeneous thermal decomposition of CH₄ [39].

To investigate the carbon formed during the methane decomposition, TG analyses of the spent samples were performed. The results in terms of percentage of carbon and temperature of the DTG peak are listed also in Table 3. As expected, in the absence of CO₂, much more carbon was accumulated over the catalysts during a shorter reaction time (about 120 min) compared to the DRM test. The Au/NiAl catalyst represented the only exception. In agreement with the TPSR curve, which showed CO continuously evolving up to 800 °C, the amount of accumulated carbon on this sample was indeed much lower than on the other samples. In all cases, the DTG peaks were in accord with the presence of graphitic carbon. The effect of the CO₂ on carbon accumulation could be inferred by a comparison of the corresponding TGA data reported in Tables 2 and 3. Indeed, the sample exhibiting a higher carbon removal temperature and higher carbon accumulation during the TPSR, i.e., Au/Ce/NiAl, was the one exhibiting a lower carbon removal temperature and a lower amount of accumulated carbon during the DRM test. Therefore, in this case, the presence of CO₂ during the DRM test contributed to the formation of an easier-to-remove carbon, favored by the close interaction between ceria and gold, enhancing the oxygen mobility of the support and the adsorption of CO₂ [40]. The Ce/NiAl maintained the same temperature for the carbon removal after TPSR and DRM, confirming the main role of ceria in favoring the formation of a more reactive carbon, regardless of the presence of CO₂. For the other two samples, NiAl and Au/NiAl, which were characterized by lower carbon removal temperatures in TPSR compared to DRM, the presence of CO₂ would not contribute to the formation of a more active carbon.

2.2. Characterization

2.2.1. BET and XRD Analyses

In Table 1, along with the elemental composition, the BET-specific surface areas and the pore volumes of the calcined HT-derived samples are listed. The particle sizes of NiO, Au and Ni as derived from the XRD analyses to be discussed later, are also included. The

N_2 adsorption–desorption isotherms are plotted in Figure 6, with the pore size distributions given in the inset.

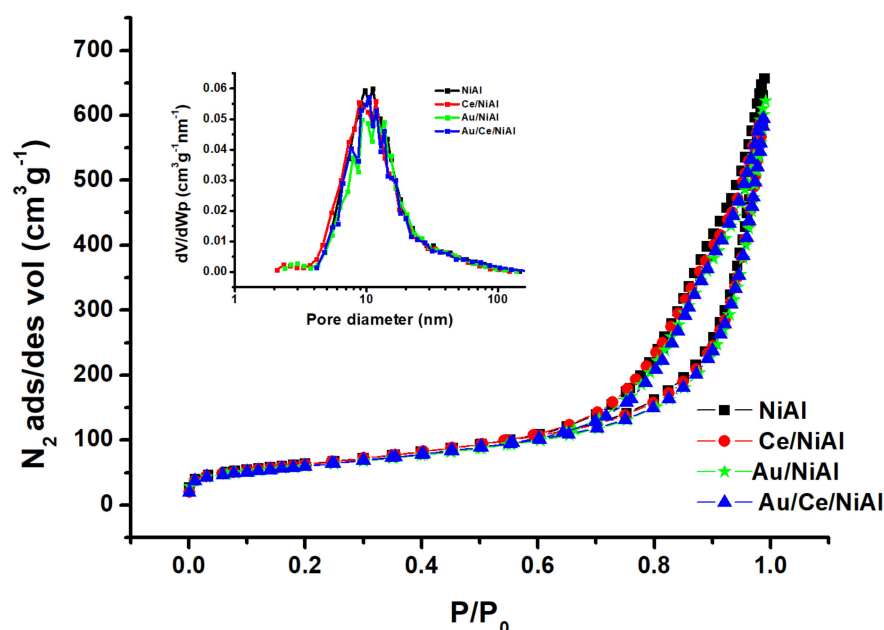


Figure 6. N_2 adsorption–desorption isotherm plots with pore size distributions in the inset of the NiAl-HT-derived catalysts.

According to the IUPAC classification, the isotherms were of type IV, characteristic of mesoporous materials, with clear hysteresis loops of H1 type [41]. With respect to the surface area of the parental hydrotalcite samples reported in the previous study, a ~70% increase in the specific surface area was observed in all the HT-derived samples [32]. The increase in the surface area was in fact expected, due to the removal of interlayer water and decomposition of the interlayer anions with the creation of additional porosity [24]. The surface areas of the gold-containing samples were slightly lower.

The structure of the parental NiAl hydrotalcites was confirmed by the X-ray diffraction patterns displayed in Figure 7, where all the reflections typical of the layered structure of takovite mineral and those of metallic gold are indicated [32].

The X-ray diffraction patterns of the catalysts, which were calcined at 600 °C, changed considerably. The diffractograms of these catalysts before and after the catalytic tests are given in Figure 8. As expected, after calcination, the takovite structure disappeared, and instead each sample before reaction exhibited a pattern characterized by the reflections at $2\theta = 37.2^\circ$, 43.3° , 62.9° , 75.4° and 79.4° indexed as (111), (200), (220), (311) and (222) crystalline planes of cubic NiO (JCDD-PDF File 00-047-1049) [42]. No peaks related to the spinel $NiAl_2O_4$ were detected. Due to the low amount of ceria, no ceria-related reflections were present in the patterns of the samples containing 1 wt% Ce. By contrast, the patterns of the samples with 3 wt% Au contained peaks at $2\theta = 38.2^\circ$ and 64.6° very close to the NiO reflections, and a peak at $2\theta = 77.5^\circ$, attributed respectively to the (111), (220) and (311) crystalline planes of the cubic Au (JCDD-PDF File 00-004-0784). Deconvolution of the NiO (111) and Au (111) peaks is shown as a zoomed-in region in the insets of Figure 8.

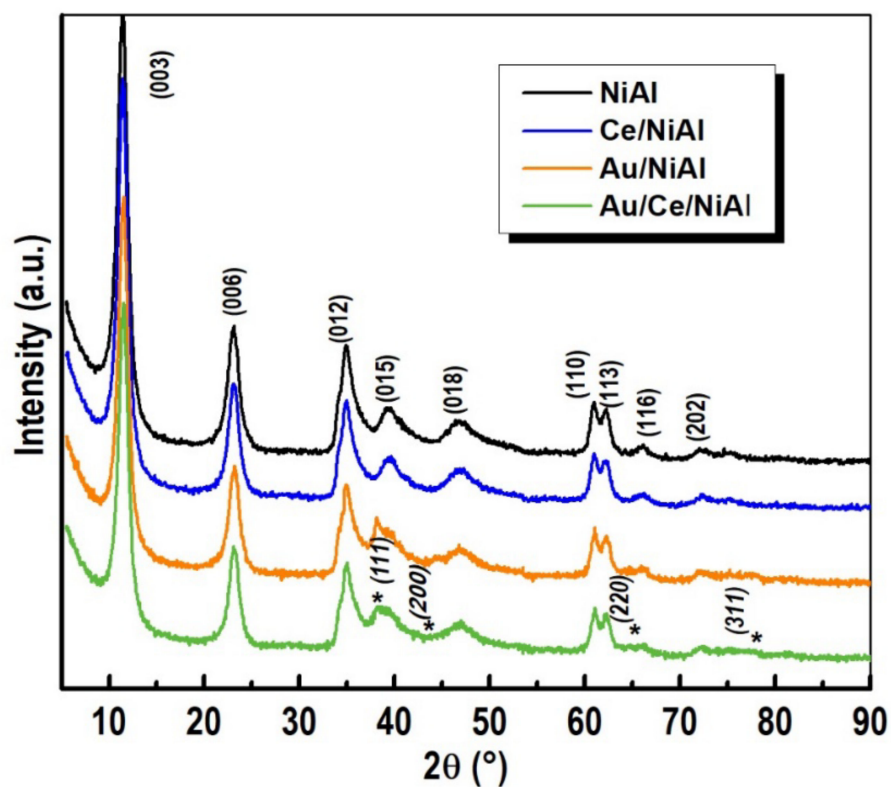


Figure 7. XRD patterns of precursor NiAl-HT samples. The diffraction lines of metallic gold are marked by asterisks.

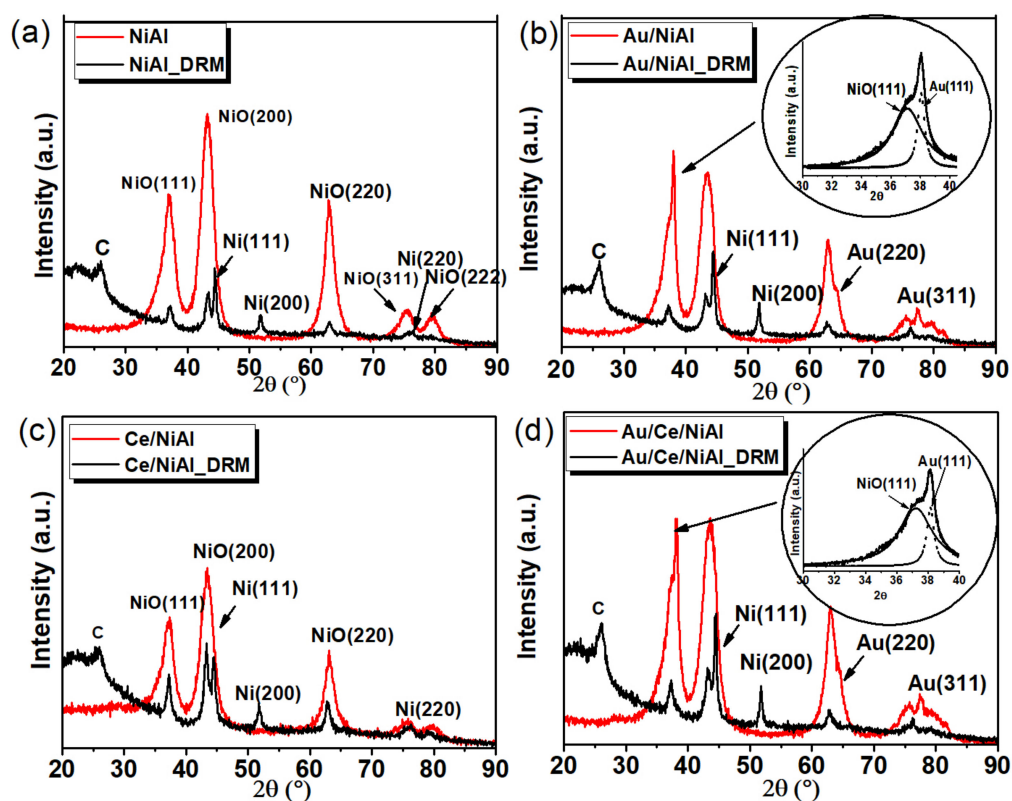


Figure 8. X-ray diffraction patterns of (a) NiAl, (b) Au/NiAl, (c) Ce/NiAl and (d) Au/Ce/NiAl HT-derived catalysts before and after DRM reaction.

The diffractograms of the spent catalysts still contained some of the strongest NiO reflections, but clearly indicated the presence of metallic nickel characterized by (111), (200) and (220) reflections at $2\theta = 44.5^\circ$, 51.8° and 76.4° , respectively (JCDD-PDF File 04-0850). Relative to the gold-containing catalysts, after the catalytic test, no gold reflections were discernible in the corresponding patterns. This could be attributed to the surface migration of gold induced by the DRM process, explaining the deactivation of the gold-containing catalysts, as discussed ahead in relation to Figure 3 [22]. From the Scherrer analyses of the NiO (200), Ni (200) and Au (111) reflections, the crystallite sizes of nickel oxide, metallic nickel and metallic gold were estimated [43]. According to the obtained values reported in Table 1, the fresh samples contained NiO particles of ~ 4 nm. In the gold-containing samples, gold crystallites of ~ 20 nm sizes were estimated. After reaction, NiO particles of larger size and Ni particles between 16 and 25 nm in size were obtained. It is worth noting that the presence of ceria limited the growth of the NiO and the Ni crystallites, whereas gold alone did not significantly affect them. A similar size-constraining effect on nickel particles exerted by ceria was reported in a WGSR investigation of similar catalysts [41]. The diffractograms of all the spent catalysts contained a peak at $2\theta \sim 26^\circ$ corresponding to graphitic carbon in accord with the TGA analyses.

2.2.2. TPR Analyses

Reforming of methane requires active sites consisting of metallic nickel aggregates, which should be readily formed and maintained during the reaction. The effect of the promoters on the reducibility of the catalysts was then investigated through H_2 -TPR analyses. The TPR profiles of the calcined catalysts are shown in Figure 9.

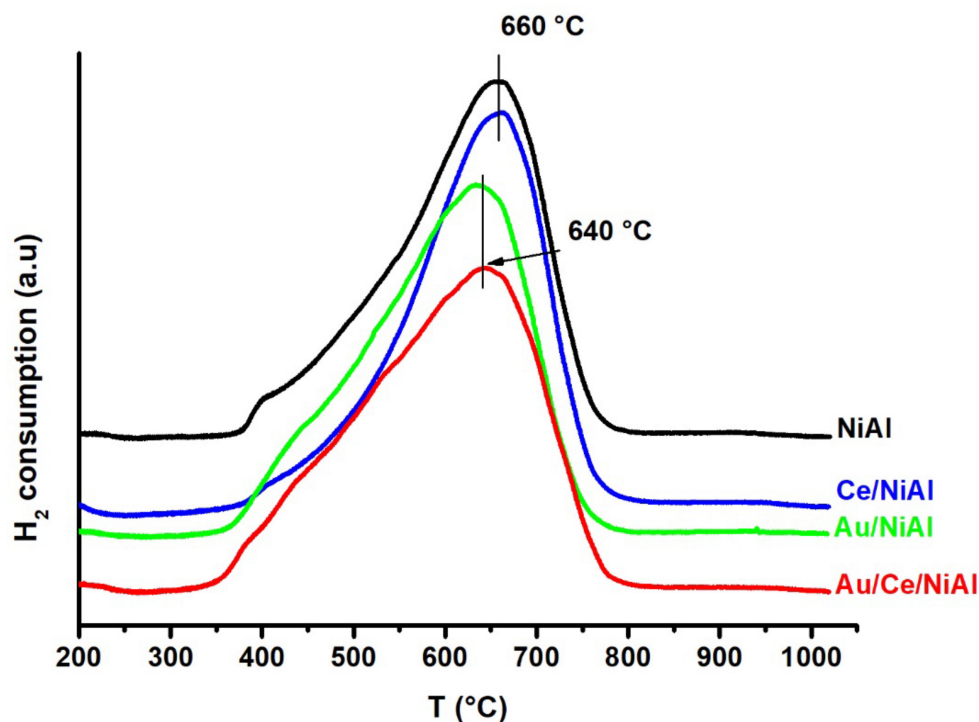


Figure 9. TPR profiles of NiAl-HT-derived catalysts.

All the profiles exhibited one broad asymmetric peak between 380°C – 800°C in accord with what is reported in literature for similar calcined NiAl HT samples [36]. The peak was attributed to the reduction of NiO in strong interaction with the alumina, whereas the asymmetry on the low-temperature side of the peak was due to the reduction of NiO particles of different sizes and differently interacting with the supports. In particular, the shoulder observed at 400°C in the profile of the NiAl could be due to larger NiO

particles less interacting with the alumina. The position of the main peak shifted from a higher temperature of 660 °C, exhibited by NiAl and CeNiAl, to 640 °C, exhibited by the Au-containing catalysts. The downward temperature shift observed in the gold-containing samples, excluding any significant particle size effect (Table 1), could be attributed to the tendency of gold to intimately interact with nickel and therefore enhancing the nickel reducibility [22]. The hydrogen consumption was different for each sample, and in all cases a little lower than the uptake of 224 ml_{H2}/g_{cat} expected from the Ni loading. With respect to the hydrogen consumption, the following order was obtained: NiAl (179 ml_{H2}/g_{cat}) < Au/NiAl = Ce/NiAl (193 ml_{H2}/g_{cat}) < Au/Ce/NiAl (210 ml_{H2}/g_{cat}). The smaller amount of hydrogen consumption, especially by the unpromoted sample, suggested the presence of some difficult-to-reduce nickel species.

2.2.3. XPS Analyses

XPS measurements of the fresh (calcined) catalysts were carried out to investigate the distribution and the chemical state of each catalyst component. The Ni 2p spectra of all the catalysts were typical of Ni²⁺, characterized by the main Ni 2p_{3/2} and Ni 2p_{1/2} spin-orbit components, each accompanied by the shakeup features [44]. As an example, the Ni 2p spectra of the Au/Ce/NiAl catalyst before (fresh) and after the DRM reaction (aged) are given in Figure 10.

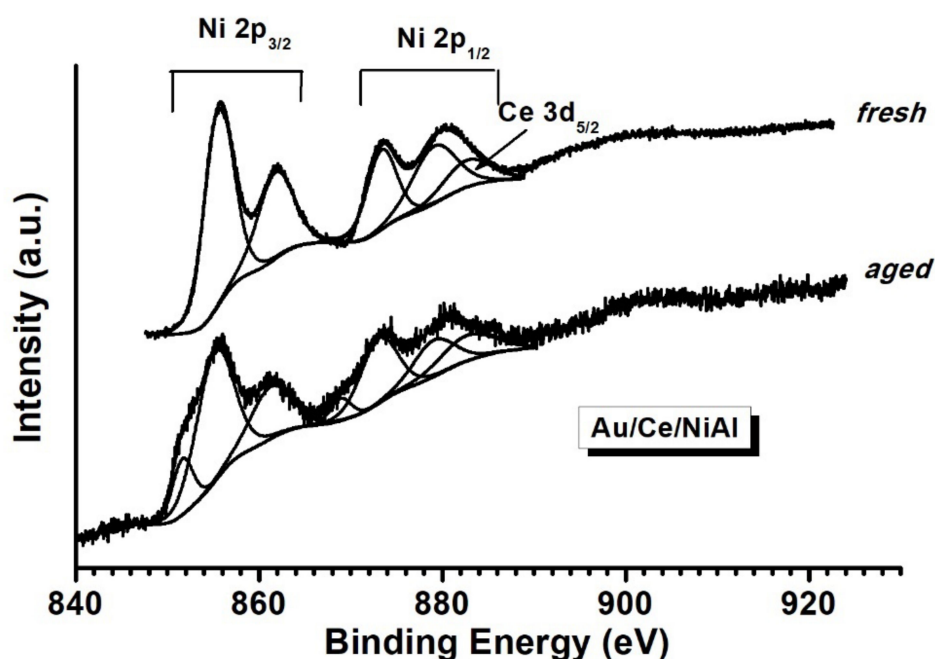


Figure 10. Ni2p XP spectra of fresh and aged AuCe/NiAl catalysts.

The main Ni 2p peaks were fitted with the two spin-orbit components Ni 2p_{3/2} and Ni 2p_{1/2} centered at 855.7 ± 0.1 eV and 873.6 ± 0.1 eV, respectively. Both peaks were accompanied by the shakeup satellites about 6 eV apart from the main photoelectron peaks. The binding energy and the presence of these satellites were typical of oxidized nickel as Ni²⁺. The Ni²⁺ in pure NiO is characterized by a Ni 2p_{3/2} binding energy of 854.5 eV, more than 1 eV smaller than the value obtained in the present case, which was intermediate between bulk NiO and NiAl₂O₄, suggesting the formation of a thin surface layer of spinel not detectable by XRD analyses. Both spectra in the figure contained extra features attributed to ceria, however the weak signals did not allow a proper fitting. After catalytic test, the intensity of the Ni 2p spectrum decreased significantly, as shown by the decreased signal-to-noise ratio. Within the uncertainty of the fitting procedure due to the

poor quality of the spectrum, it was possible to fit small components attributed to metallic nickel characterized by Ni 2p_{3/2} binding energy at ~851.8 eV.

In Figure 11, the spectral regions of the fitted Ni 3p, Al 2p and Au 4f are displayed. The binding energy of Al 2p was equal to 74.5 eV ± 0.1 eV, which is typical of aluminum oxide. The binding energy of Au 4f_{7/2} of 84.0 eV obtained in both gold-containing samples was typical of metallic gold [22]. The extra peak overlapping with the Au 4f_{5/2} component was due to an Al 2p plasmon satellite. The fitting allowed a proper quantification of the elements in terms of atomic ratios. The results for all the fresh catalysts in terms of binding energies and atomic ratios are summarized in Table 4.

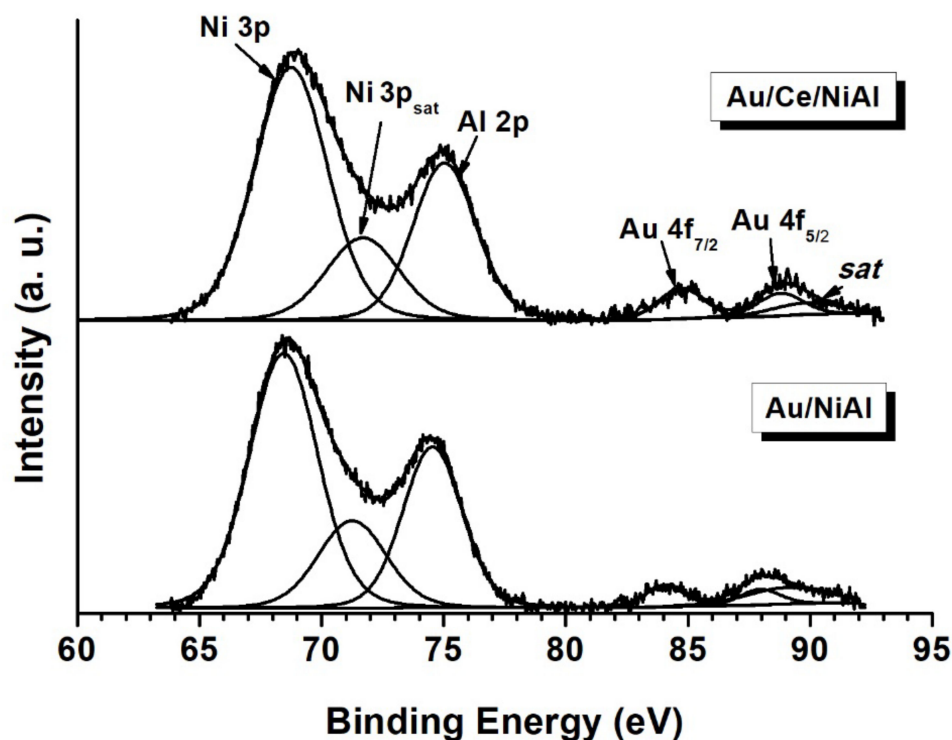


Figure 11. Background subtracted X-ray photoelectron regions of Ni 3p, Al2p and Au4f spectra for the fresh gold-containing samples.

Table 4. XPS binding energies (eV) and XPS-derived atomic ratios of the HT-derived samples.

Samples	Ni 2p _{3/2} (eV)	Ni 3p (eV)	Au 4f _{7/2} (eV)	Al 2p (eV)	Ni/Al XPS *	Au/Al XPS *
NiAl	855.7	68.6		74.6	0.5 (2.5)	-
Au/NiAl	855.8	68.4	84.0	74.5	0.6 (2.5)	0.004 (0.036)
Ce/NiAl	855.6	68.4		74.5	0.7 (2.5)	-
Au/Ce/NiAl	855.6	68.5	84.0	74.6	0.6 (2.5)	0.007 (0.037)

* The values in parentheses correspond to the bulk analytical ratios.

From the comparison of the XPS-derived surface atomic ratios Ni/Al_{XPS} and Au/Al_{XPS} with the corresponding bulk ratios, a surface depletion of nickel and gold was evident. This observation could have been a direct consequence of the migration of both metals inside the hydrotalcite structure during the precursor's preparation procedure and during the calcination. It is worth noting the surface enhancement of nickel in the ceria- and gold-promoted catalysts, which explains their better initial activity with respect to the unpromoted one. Moreover, an enrichment of the surface gold concentration due to the presence of ceria was observed in the Au/Ce/NiAl catalyst. As shown in Figure 12 for the Au/Ce/NiAl sample, in accordance with the XRD patterns and the TGA analyses, a strong

and asymmetric C 1s peak at ~284 eV typical of graphitic carbon was observed in all the C 1s regions of the spent catalysts [44]. Unfortunately, after the catalytic test, the extensive deposition of carbon over the samples prevented the XP analyses of the Au 4f peaks.

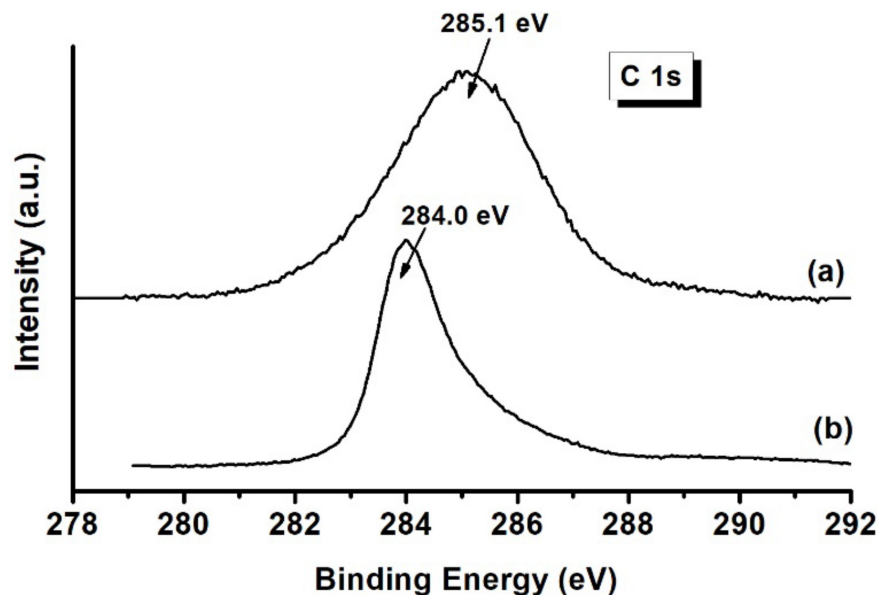


Figure 12. C 1s XP spectra of Au/Ce/NiAl; (a) before and (b) after DRM.

3. Experimental

3.1. Synthesis of Materials

The materials were prepared according to the procedure already described [32]. In brief, the carbonate form of NiAl-HT with a $\text{Ni}^{2+}/\text{Al}^{3+}$ molar ratio of 2.5 was obtained by coprecipitating at 80 °C and at constant pH = 8 the mixed aqueous solution of 0.5M $\text{Ni}(\text{NO}_3)_2 \times 6\text{H}_2\text{O}$, and $\text{Al}(\text{NO}_3)_3 \times 9\text{H}_2\text{O}$ with a 0.9M Na_2CO_3 as precipitant agent. The obtained slurry was aged for 60 min under controlled stirring conditions, filtered off and washed with hot distilled water. Then, the precipitate was dried at 105 °C for 20 h.

The CeO_2 -modified NiAl-HT sample, containing 1wt.% CeO_2 , was prepared by the direct deposition of ceria over the NiAl-HT suspended in distilled water, through precipitation of Ce^{3+} ions from $\text{Ce}(\text{NO}_3)_3 \times 6\text{H}_2\text{O}$ with 1M NaOH. The washed sample (pH of filtrate ~6–7) was dried at 105 °C.

Gold-containing samples were obtained by deposition–precipitation of gold over NiAl-HT and Ce/NiAl-HT. Portions of the HT powders were homogeneously suspended in distilled water with the help of ultrasound. Deposition of gold (3 wt.%) was performed by simultaneous addition of aqueous solutions of 0.06 M $\text{HAuCl}_4 \times 3\text{H}_2\text{O}$ and 0.2 M Na_2CO_3 into the reactor at 60 °C and pH = 7.0. After aging under the same conditions, for 60 min, the samples were filtered and carefully washed with distilled water until the removal of the Cl^- ions.

The elemental composition of each sample, as obtained from ICP measurements, is listed in Table 1. The molar ratio of $\text{Ni}^{2+}/\text{Al}^{3+}$ of the promoted and unpromoted samples satisfied the range of $0.2 < \text{M}^{2+}/(\text{M}^{2+} + \text{M}^{3+}) < 0.33$ required for the formation of pure hydroxaltes [28]. Formation of the layered double-oxide structure NiAl-HT was confirmed by the X-ray diffraction pattern typical of the mineral takovite, as previously reported [32]. For the catalytic application, all the samples were calcined at 600 °C for 2 h with a heating rate of 5 °C/min, and they were designated as NiAl, Ce/NiAl, Au/NiAl and Au/Ce/NiAl.

3.2. Characterization

Specific surface areas and pore volumes of the samples were measured at –196 °C with a nitrogen sorption technique using the ASAP 2020 equipment (Micromeritics, Norcross,

GA, USA). Before the measurements, the powder samples were degassed at 250 °C for 2 h. The specific surface area was calculated via the Brunauer-Emmett-Teller (BET) method in the standard pressure range 0.05–0.3 P/P⁰. The pore volume and pore size distribution were obtained by analysis of the desorption branch, using the Barrett, Joyner and Halenda (BJH) calculation method [41].

X-ray diffraction (XRD) patterns were recorded with a D5000 diffractometer (Bruker AXS, Karlsruhe, Germany) employing Ni-filtered Cu K α radiation in the 2 θ range between 20° and 90° with 0.05° step size. The assignment of the crystalline phases was based on the JPDFS powder diffraction file cards [42]. Crystallite sizes were calculated from the Scherrer analyses of selected peaks [43].

H₂ temperature-programmed reduction (TPR) measurements were carried out with Autochem 2910 HP system (Micromeritics, Norcross, GA, USA) equipped with a TCD detector. Before analysis, 0.1 g of the sample was treated with a mixture of 5% O₂/He (*v/v*, 50 mL/min) while heating up (10 °C/min) to 400 °C, and was left at this temperature for 30 min. After cooling to room temperature, the gas mixture of 5% H₂/Ar (*v/v*, 30 mL/min) was introduced into the sample tube. The hydrogen consumption was measured as a function of the temperature, increased up to 1000 °C at a rate of 10 °C/min.

The X-ray photoelectron spectroscopy (XPS) analyses were carried out with a VG Microtech ESCA 3000 Multilab (VG Scientific, Sussex, UK), equipped with a dual Mg/Al anode. Al K α radiation was used as an excitation source (1486.6 eV). All the binding energies were referred to the C 1s energy, previously calibrated at 285.1 eV, arising from adventitious carbon. Qualitative and quantitative analyses of the peaks were performed using CasaXPS software (version 2.3.17, Casa Software Ltd. Wilmslow, Cheshire, UK, 2009). A precision of ± 0.15 eV on the binding energy values and of $\pm 10\%$ on the atomic percentages was considered.

The thermogravimetric analyses (TGA) of the samples after the catalytic reactions were performed using the TGA 1 Star System (Mettler Toledo, Schwerzenbach, Switzerland). About 10 mg of the sample were heated from room temperature to 100 °C, left at this temperature for 1 h and then heated to 1100 °C at the rate of 10 °C/min under flowing air at 30 mL/min.

3.3. Catalytic Measurements

The DRM reaction was carried out in a fixed-bed quartz reactor with an inner diameter of 12 mm. The reaction was conducted under atmospheric pressure in the temperature range of 450 °C–700 °C, with increasing temperature steps of 50 °C. Typically, 10 mg of catalyst powder (sieved fraction between 180 and 250 μ m) diluted 1:2 with inert SiC were placed inside the reactor. Then, prior to the catalytic testing, to clean up the catalyst surface and make consistent comparisons between the different catalysts, the samples were treated with a mixture of 5% O₂/He (*v/v*, 50 mL/min) at 350 °C for 1/2 h. After cooling down to room temperature, the sample was heated up to 750 °C at a rate of 10 °C/min in a 5% H₂/He (*v/v*, 30 mL/min), and held at this temperature for 1 h. The feed gas composed of 10% of CH₄, 10% of CO₂ and He as balance was introduced into the reactor with a flow rate of 100 mL/min (STP), equivalent to a gas hourly space velocity (GHSV) of 600,000 mL g⁻¹ h⁻¹. The inlet and outlet gas compositions were analyzed online using the Agilent 7890B Gas Chromatograph (Agilent Technology, Santa Clara, CA, USA) equipped with a DB-1 capillary column and a molecular sieve, to follow the evolution of CH₄, CO, CO₂ and H₂, using FID and TCD detectors. Water was condensed at the outlet of the reactor. CH₄ and CO₂ conversion, X_{CH_4} and X_{CO_2} respectively, and hydrogen yield Y_{H_2} (%) were calculated according to the following equations, where CH₄ⁱⁿ, CO₂ⁱⁿ and CH₄^{out}, CO₂^{out}, H₂^{out} refer to the concentration (ppm) of the species entering and exiting, respectively, the catalytic reactor.

$$X_{\text{CH}_4} = 100 \times (\text{CH}_4^{\text{in}} - \text{CH}_4^{\text{out}}) / \text{CH}_4^{\text{in}}$$

$$X_{\text{CO}_2} = 100 \times (\text{CO}_2^{\text{in}} - \text{CO}_2^{\text{out}}) / \text{CO}_2^{\text{in}}$$

$$Y_{\text{H}_2} (\%) = 100 \times \text{H}_2^{\text{out}} / (2 \times \text{CH}_4^{\text{in}})$$

The activation of methane by the catalyst surface was investigated by temperature-programmed surface reaction of methane (TPSR-CH₄), using Autochem 2950 HP system (Micromeritics, Norcross, GA, USA). For this reaction, 10 mg of catalyst mixed with 1 g of carborundum to disperse the active phase were placed in a U-shaped quartz tube with quartz wool on each side of the bed. Before the reaction, the sample underwent the same oxidation and reduction treatment used for the DRM reaction, as described above. After pretreatment, the sample was cooled down to room temperature in He. Then, a mixture of 5% CH₄/He (*v/v*, 30 mL/min) was introduced into the reactor, and the temperature was increased up to 1100 °C, using a heating rate of 10 °C/min. The evolutions of CH₄, CO₂ and CO were registered using UV/IR analyzers (ABB S.p.a. Milano, Italy).

4. Conclusions

Ni containing hydrotalcite-derived catalysts with a molar ratio Ni⁺⁺/Al⁺⁺⁺ ratio = 2.5 were used in the dry reforming of methane. The samples were modified by the addition of cerium and gold to improve the resistance of the catalyst toward carbon formation and toward sintering of the nickel. The unpromoted and promoted catalysts were tested at a relatively low temperature range between 450 °C and 700 °C. Values of CH₄ conversion between 67% and 74% obtained at 700 °C under the harsh experimental condition of a high space velocity (600,000 mL g⁻¹ h⁻¹) were indicative of active catalysts. During the temperature-dependent DRM test, definite improvement in the CH₄ conversion of the promoted catalysts compared to the unpromoted NiAl was observed, particularly of the Au/Ce/NiAl containing both promoter elements. The H₂/CO molecular ratio decreased with temperature, ranging from values above 1.5 to a stable 0.7 for temperatures above 600 °C. The changes in the H₂/CO ratio along with the discrepancies between the CH₄ and CO₂ conversions were related to side reactions taking place during the DRM test. During 6 h of time on stream at 700 °C, all catalysts deactivated, the Ce/NiAl to a lesser degree and the two gold-containing samples to a greater degree. Accumulation of graphitic carbon, observed in all the spent catalysts, contributed to the deactivation.

The present study confirmed that the formation of carbon, acknowledged as one of the main causes of the nickel catalyst deactivation, was not always deleterious. The presence of ceria, which in the present case did not prevent the formation of carbon, contributed to an enhancement of the catalytic activity stability due to a particle-size-constraining effect. The gold-containing catalysts, in spite of similar or even lower amounts of registered carbon after DRM reaction, deactivated the most, due to the gold surface segregation driven by the reaction conditions. Moreover, a lower carbon-removal temperature observed in the TGA analyses of the spent promoted catalysts must be considered beneficial from the perspective of the catalyst regeneration procedure. Particularly in the case of the Au/Ce/NiAl catalyst, the close interaction between gold and ceria enhancing the oxygen mobility of the support and the adsorption of CO₂ would favor the removal of the formed carbon. Therefore, any preparation method that allows proper anchoring of the gold in the catalyst structure, inhibiting its surface segregation, could be promising for obtaining a catalyst with better DRM performance.

Author Contributions: Conceptualization, A.M.V. and T.T.; methodology, V.L.P. and A.M.V.; catalytic activity, V.L.P. and G.P.; characterization and TPR/TPO measurements, L.F.L. and G.P.; XPS analyses, A.M.V. and V.L.P.; synthesis, M.G., D.N. and T.T.; writing and editing, A.M.V. and G.P. All the authors contributed to the data discussion and manuscript preparation. All authors have read and agreed to the published version of the manuscript.

Funding: The authors kindly acknowledge financial support from the Bilateral Project between the CNR and the Bulgarian Academy of Science (BAS). Authors affiliated with the ISMN-CNR acknowledge funding from the National Project NAUSICA (ARS01_00334-CUP B45F21000680005) and from the PNRR—Missione 2 “Rivoluzione Verde e Transizione Ecologica”—Componente 2

“Energia Rinnovabile, Idrogeno, Rete e Mobilità Sostenibile”—Investimento 3.5 “Ricerca e Sviluppo sull’Idrogeno”—Decreto MITE n. 545 del 23/12/2021(AdC ENEA-CNR) (CUP B93C22000630006). Authors affiliated with the Institute of Catalysis-BAS gratefully acknowledge the support of the European Regional Development Fund within the Operational Programme “Science and Education for Smart Growth 2014–2020”, Project CoE “National Center of Mechatronics and Clean Technologies “BG05M2OP001-1.001-0008”.

Data Availability Statement: The data presented in this study are available in the article.

Acknowledgments: Administrative support by Giovanna Bellanti, Giuseppe Napoli and Salvatore Romeo is acknowledged. The authors are thankful to Francesco Giordano for performing XRD analyses and to Nunzio Galli for performing surface area measurements.

Conflicts of Interest: The authors declare no conflict of interest.

References

1. Wittich, K.; Krämer, M.; Bottke, N.; Schunk, S.A. Catalytic Dry Reforming of Methane: Insights from Model Systems. *ChemCatChem* **2020**, *12*, 2130–2147. [[CrossRef](#)]
2. Seo, H.O. Recent Scientific Progress on Developing Supported Ni catalysts for Dry (CO₂) Reforming of Methane. *Catalysts* **2018**, *8*, 11. [[CrossRef](#)]
3. Cai, X.; Hu, Y.H. Advances in catalytic conversion of methane and carbon dioxide to highly valuable products. *Energy Sci. Eng.* **2019**, *7*, 4–29. [[CrossRef](#)]
4. Gao, X.; Ge, Z.; Zhu, G.; Wang, Z.; Ashok, J.; Kawi, S. Anti-Coking and Anti-Sintering Ni/Al₂O₃ Catalysts in the dry reforming of methane: Recent Progress and Prospects. *Catalysts* **2021**, *11*, 1003. [[CrossRef](#)]
5. Sandoval-Diaz, L.E.; Schlögl, R.; Lunkenbein, T. Quo Vadis Dry Reforming of Methane? A Review on Its Chemical, Environmental, and Industrial Prospects. *Catalysts* **2022**, *12*, 465. [[CrossRef](#)]
6. Touma, J.G.; Tarboush, B.A.; Zeaiter, J.; Ahmad, M.N. Catalyst design for dry reforming of methane: Analysis Reviews. *Renew. Sustain. Energy Rev.* **2018**, *82*, 2570–2583.
7. Parsapur, R.K.; Chatterjee, S.; Huang, K.-W. The Insignificant Role of Dry Reforming of Methane in CO₂ Emission Relief. *ACS Energy Lett.* **2020**, *5*, 2881–2885. [[CrossRef](#)]
8. Arora, S.; Prasad, R. An overview on dry reforming of methane: Strategies to reduce carbonaceous deactivation of catalysts. *RSC Adv.* **2016**, *6*, 108688. [[CrossRef](#)]
9. Muraza, O.; Galadima, A. A review on coke management during dry reforming of methane. *Int. J. Energy Res.* **2015**, *39*, 1196–1216. [[CrossRef](#)]
10. Bermúdez, J.; Fidalgo, B.; Arenillas, A.; Menéndez, J. Dry reforming of coke oven gases over activated carbon to produce syngas for methanol synthesis. *Fuel* **2010**, *89*, 2897–2902. [[CrossRef](#)]
11. Han, J.W.; Park, J.S.; Choi, M.S.; Lee, H. Uncoupling the size and support effects of Ni catalysts for dry reforming of methane. *Appl. Catal. B* **2017**, *203*, 625–632. [[CrossRef](#)]
12. Akri, M.; Zhao, S.; Li, X.; Zang, K.; Lee, A.F.; Isaacs, M.A.; Xi, W.; Gangarajula, Y.; Luo, J.; Ren, Y.; et al. Atomically dispersed nickel as coke-resistant active sites for methane dry reforming. *Nat. Commun.* **2019**, *10*, 5181. [[CrossRef](#)] [[PubMed](#)]
13. Vogt, C.; Kranenborg, J.; Monti, M.; Weckhuysen, B.M. Structure Sensitivity in Steam and Dry Reforming over Nickel: Activity and Carbon formation. *ACS Catal.* **2020**, *10*, 1428–1438. [[CrossRef](#)]
14. Xu, Y.; Du, X.-H.; Li, J.; Wang, P.; Zhu, J.; Ge, F.-J.; Zhou, J.; Song, M.; Zhu, W.-Y. A comparison of Al₂O₃ and SiO₂ supported Ni-based catalysts on their performance for the dry reforming of methane. *J. Fuel Chem. Technol.* **2019**, *47*, 199–208. [[CrossRef](#)]
15. Singh, R.; Dhir, A.; Mohapatra, S.K.; Mahia, S.K. Dry reforming of methane using various catalysts in the process: Review. *Biomass Convers. Biorefinery* **2020**, *10*, 567–587. [[CrossRef](#)]
16. Emamdoust, A.; La Parola, V.; Pantaleo, G.; Testa, M.L.; Farjami Shayesteh, S.; Venezia, A.M. Partial oxidation of methane over SiO₂ supported Ni and NiCe catalysts. *J. Energy Chem.* **2020**, *47*, 1–9. [[CrossRef](#)]
17. Marinho, A.L.A.; Toniolo, F.S.; Noronha, F.B.; Epron, F.; Duprez, D.; Bion, N. Highly active and stable Ni dispersed on mesoporous CeO₂-Al₂O₃ catalysts for production of syngas by dry reforming of methane. *Appl. Catal. B* **2021**, *10*, 1428–1438. [[CrossRef](#)]
18. Yang, R.; Xing, C.; Lv, C.; Shi, L.; Tsubaki, N. Promotional effect of La₂O₃ and CeO₂ on Ni/gAl₂O₃ catalysts for CO₂ reforming of CH₄. *Appl. Catal. A* **2010**, *385*, 92–100. [[CrossRef](#)]
19. Wang, Y.; Yao, L.; Wang, Y.; Wang, S.; Zhao, Q.; Mao, D.; Hu, C. Low -Temperature Catalytic CO₂ Dry Reforming of Methane on Ni-Si/ZrO₂ catalyst. *ACS Catal.* **2018**, *8*, 6495–6506. [[CrossRef](#)]
20. Pantaleo, G.; La Parola, V.; Testa, M.L.; Venezia, A.M. CO₂ reforming of CH₄ over SiO₂-Supported Ni Catalyst: Effect of Sn as Support and metal Promoter. *Ind. Eng. Chem. Res.* **2021**, *60*, 18684–18694. [[CrossRef](#)]
21. Horváth, A.; Beck, A.; Maróti, B.; Sáfrán, G.; Pantaleo, G.; Liotta, L.F.; Venezia, A.M.; La Parola, V. Strong impact of indium promoter on Ni/Al₂O₃ and Ni/CeO₂-Al₂O₃ catalysts used in dry reforming of methane. *Appl. Catal. A* **2021**, *621*, 18174. [[CrossRef](#)]

22. Horváth, A.; Guzzi, L.; Kocsonya, A.; Sáfrán, G.; La Parola, V.; Liotta, L.F.; Pantaleo, G.; Venezia, A.M. Sol-derived AuNi/MgAl₂O₄ catalysts: Formation, structure and activity in dry reforming of methane. *Appl. Catal. A* **2013**, *468*, 250–259. [[CrossRef](#)]
23. Bhatar, S.; Abedin, M.A.; Kanitkar, S.; Spivey, J.J. A review on dry reforming of methane over perovskite derived catalysts. *Catal. Today* **2021**, *365*, 2–23. [[CrossRef](#)]
24. Debeğ, R.; Motak, M.; Grzybek, T.; Galvez, M.E.; Da Costa, P. A short review on the Catalytic Activity of Hydrotalcite-Derived Materials for Dry Reforming of Methane. *Catalysts* **2017**, *7*, 32. [[CrossRef](#)]
25. Marcu, I.-C.; Pavel, O.D. Layered Double Hydroxide-Based Catalytic Materials for Sustainable Processes. *Catalysts* **2022**, *12*, 816. [[CrossRef](#)]
26. Abdelsadek, Z.; Holgado, J.P.; Halliche, D.; Caballero, A.; Cherifi, O.; Cortes, S.G.; Masset, P.J. Examination of the deactivation Cycle of NiAl and NiMgAl-Hydrotalcite derived catalysts in the Dry Reforming of Methane. *Catal. Lett.* **2021**, *151*, 2596–2715. [[CrossRef](#)]
27. Dai, H.; Zhu, Y.; Xiong, S.; Xiao, X.; Huang, L.; Deng, J.; Zhou, C. Dry Reforming of Methane over Ni/MgO@Al Catalysts with Unique Feature of Sandwich Structure. *Chem. Sel.* **2021**, *6*, e202102788. [[CrossRef](#)]
28. Touahra, F.; Sehaïlia, M.; Ketir, W.; Bachari, K.; Chebout, R.; Tarri, M.; Cherifi, O.; Halliche, D. Effect of the Ni/Al ratio of Hydrotalcite-type catalysts on their performance in the methane dry reforming process. *Appl. Petrochem. Res.* **2016**, *6*, 1–13. [[CrossRef](#)]
29. Daza, C.E.; Gallego, J.; Mondragon, F.; Moreno, S.; Molina, R. High stability of Ce-promoted Ni/Mg-Al catalysts derived from Hydrotalcites in dry reforming of methane. *Fuel* **2010**, *89*, 592–603. [[CrossRef](#)]
30. Lucredio, A.F.; Assaf, J.M.; Assaf, E.M. Reforming of a model sulfur-free biogas on Ni catalysts supported on Mg(Al)O derived from hydrotalcite precursors: Effect of La and Rh addition. *Biomass Bioenergy* **2014**, *60*, 8–17. [[CrossRef](#)]
31. Bhattacharyya, A.; Chang, V.W.; Schumaker, D.J. CO₂ reforming of methane to syngas; I: Evaluation of Hydrotalcite clay-derived catalysts. *Appl. Clay Sci.* **1998**, *13*, 317–328. [[CrossRef](#)]
32. Gabrovska, M.; Ivanov, I.; Nikolova, D.; Krstic, J.; Venezia, A.M.; Crisan, D.; Crisan, M.; Tenchev, K.; Idakiev, V.; Tabakova, T. Improved Water–Gas Shift Performance of Au/NiAl LDHs Nanostructured Catalysts via CeO₂ Addition. *Nanomaterials* **2021**, *11*, 366. [[CrossRef](#)] [[PubMed](#)]
33. Ali, S.; Khader, M.M.; Almarri, M.; Abdelmoneim, A.G. Ni-Based Catalysts for the dry reforming of methane. *Catal. Today* **2020**, *343*, 26–37. [[CrossRef](#)]
34. Nikoo, M.K.; Amin, N.A.S. Thermodynamic analysis of carbon dioxide reforming in view of solid carbon formation. *Fuel Process. Technol.* **2011**, *92*, 678–691. [[CrossRef](#)]
35. Wang, Y.; Li, L.; Cui, C.; Da Costa, P.; Hu, C. The effect of absorbed oxygen species on carbon-resistance of Ni-Zr catalyst modified by Al and Mn for dry reforming of methane. *Catal. Today* **2022**, *384–386*, 257–264.
36. Debeğ, R.; Motak, M.; Grzybek, T.; Galvez, M.E.; Da Costa, P. Catalytic activity of hydrotalcite-derived catalysts in the dry reforming of methane: The effect of Ce promotion and feed gas composition. *React. Kinet. Mech. Catal.* **2017**, *121*, 185–208. [[CrossRef](#)]
37. Guil-Lopez, R.; La Parola, V.; Pena, M.A.; Fierro, J.L.G. Evolution of the Ni-active centres into ex Hydrotalcite oxide catalysts during the CO_x-free hydrogen production by methane decomposition. *Int. J. Hydrogen Energy* **2012**, *37*, 7042–7705. [[CrossRef](#)]
38. Zhang, M.; Zhang, J.; Wu, Y.; Pan, J.; Zhang, Q.; Tan, Y.; Han, Y. Insight into the effects of the oxygen species over Ni/ZrO₂ catalyst surface on methane reforming with carbon dioxide. *Appl. Catal. B* **2019**, *244*, 427–437. [[CrossRef](#)]
39. Pantaleo, G.; La Parola, V.; Deganello, F.; Singha, R.K.; Bal, R.; Venezia, A.M. Ni/CeO₂ catalysts for methane partial oxidation: Synthesis, driven structural and catalytic effects. *Appl. Catal. B* **2016**, *189*, 233–241. [[CrossRef](#)]
40. Tabakova, T.; Gabrovska, M.; Nikolova, D.; Ivanov, I.; Venezia, A.M.; Tenchev, K. Exploring the role of promoters (Au, Cu and Re) in the performance of Ni-Al layered double hydroxides for water-gas shift reaction. *Int. J. Hydrog. Energy* **2022**, *in press*. [[CrossRef](#)]
41. Thommes, M.; Kaneko, K.; Neimark, A.V.; Olivier, J.P.; Rodriguez-Reinoso, F.; Rouquerol, J.; Sing, K.S.W. Physisorption of Gases, with Special Reference to the Evaluation of Surface Area and Pore Size Distribution (IUPAC Technical Report). *Pure Appl. Chem.* **2015**, *87*, 1051–1069. [[CrossRef](#)]
42. *Inorganic Crystal Structure Database (ICSD)*; FIZ Karlsruhe, GmbH: Eggenstein-Leopoldshafen, Germany, 2014.
43. Klug, H.P.; Alexander, L.E. *X-Ray Diffraction Procedures for Polycrystalline and Amorphous Materials*, 2nd ed.; John Wiley and Sons: New York, NY, USA, 1974.
44. La Parola, V.; Liotta, L.F.; Pantaleo, G.; Testa, M.L.; Venezia, A.M. CO₂ reforming of CH₄ over Ni supported on SiO₂ modified by TiO₂ and ZrO₂: Effect of the support synthesis procedure. *Appl. Catal. A* **2022**, *642*, 118704. [[CrossRef](#)]

Disclaimer/Publisher’s Note: The statements, opinions and data contained in all publications are solely those of the individual author(s) and contributor(s) and not of MDPI and/or the editor(s). MDPI and/or the editor(s) disclaim responsibility for any injury to people or property resulting from any ideas, methods, instructions or products referred to in the content.